iScience

CellPress
OPEN ACCESS

Article

Differential fate between oxytocin and vasopressin cells in the developing mouse brain

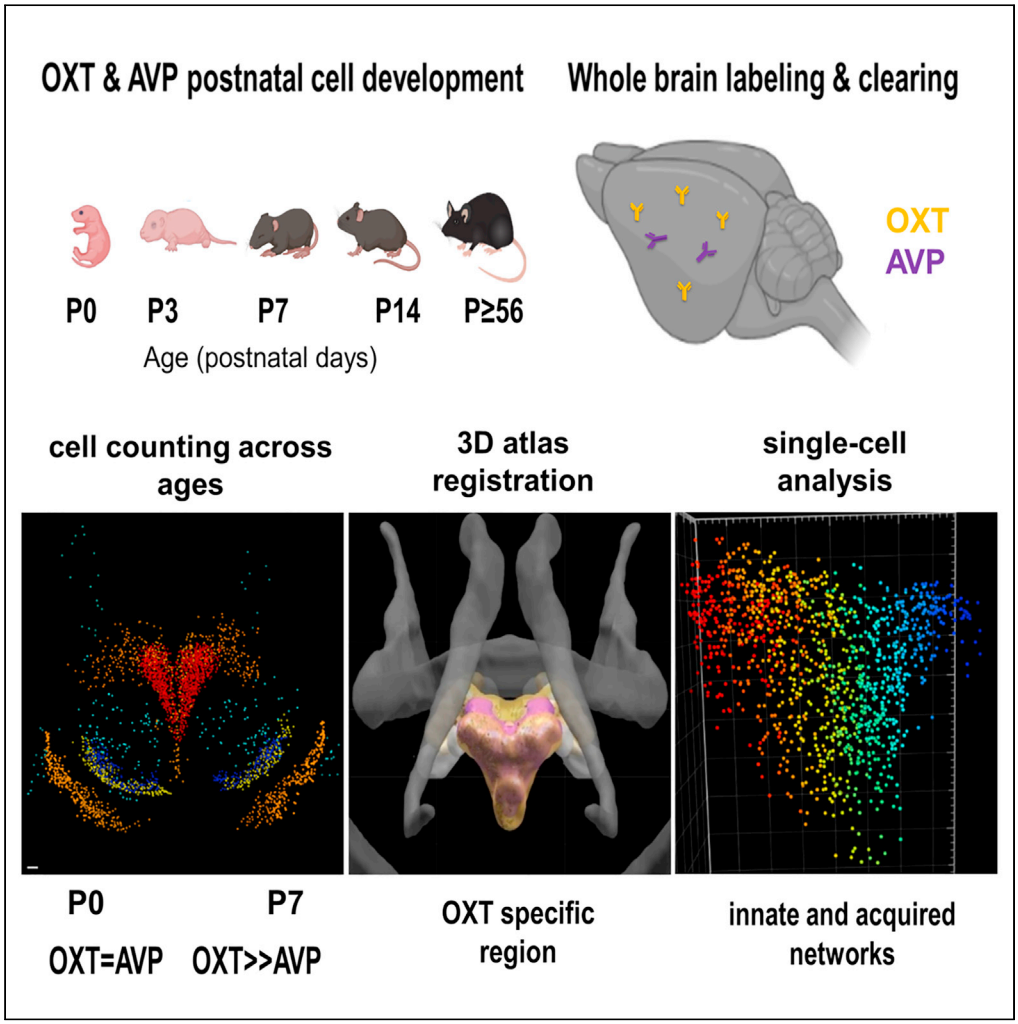

Amelie Soumier, Marie Habart, Guillaume Lio, Caroline Demily, Angela Sirigu

angela.sirigu@isc.cnrs.fr

Highlights

The OXT system continues to mature during early development but not the AVP system

OXT hypothalamic nuclei emerge at different rates after birth

PVN cells gradually acquire an oxytocinergic phenotype

OXT cells are organized into innate and adaptive neural networks

Soumier et al., iScience *25*, 103655
January 21, 2022
https://doi.org/10.1016/j.isci.2021.103655

iScience

CellPress
OPEN ACCESS

Article

Differential fate between oxytocin and vasopressin cells in the developing mouse brain

Amelie Soumier,[1,2,3] Marie Habart,[1,2,3] Guillaume Lio,[1,2] Caroline Demily,[1,2] and Angela Sirigu[1,2,4,*]

SUMMARY

Oxytocin (OXT) and arginine vasopressin (AVP), two neuropeptides involved in socio-emotional behaviors have been anatomically defined in the adult brain. Yet their spatial organization during postnatal development is not clearly defined. We built a developmental atlas using 3D imaging of cleared immunolabeled tissue over four early postnatal (P) stages, from birth (P0, P3, P7, P14) to young adulthood (≥P56). Our atlas-based mapping revealed that the number of OXT neurons doubles according to unique temporal dynamics in selective hypothalamic regions, namely, the periventricular and paraventricular nuclei, and in a novel location we named the antero-lateral preoptic. In the paraventricular nucleus, single-cell densities and fluorescence analysis demonstrated selective expansion of OXT cells in the antero-ventral division, whereas the postero-dorsal division contained cells present at birth. No changes were observed for AVP neurons. Our findings show the coexisting of innate and plastic OXT/AVP brain circuits probably triggered by environmental adaptation of the social brain.

INTRODUCTION

Oxytocin (OXT) and its partner arginine vasopressin (AVP) are neuropeptides that are essentials for regulating species- and sex-specific social behaviors. Decades of research in human and in animal models has demonstrated their involvement in social recognition and memory, parental behaviors, social bonding, and cooperation (Donaldson and Young, 2008). As such, they play critical roles in typically developing individuals (Andari et al., 2014; Johnson and Young, 2017). They are also thought to be implicated in neurodevelopmental disorders including autism, social anxiety, and schizophrenia (Andari et al., 2016; Grinevich and Neumann, 2021; Lefevre and Sirigu, 2016). The relationship between the OXT and AVP systems was initially described as antagonistic, in which OXT supports pro-social behaviors, underlying interpersonal attachment, and trust, whereas AVP supports individual defensive behaviors, including mobilization and aggression. This opposite behavioral function has since been challenged, as a growing body of evidence indicates that social engagement is likely supported by the dynamic coordination of OXT and AVP neural networks (Rae et al., 2021; Stoop, 2012). With respect to this idea, OXT and AVP are able to bind to each other's specific receptor (Carter, 2017; Song and Albers, 2018). In addition, the distribution of OXT and AVP receptors shows mostly distinct and non-overlapping expression (Dumais and Veenema, 2016; Song and Albers, 2018) suggesting that these two neural systems are key components of the same signaling pathway, having either complementary or opposing functional roles depending on the species, sex, age, and social experiences.

Given the importance of the balance of OXT/AVP over social function, it becomes increasingly important to identify the sensitive developmental periods that favor the emergence of such relationship. Studies have identified that the early postnatal period is critical for the development of social skills and the development of OXT and AVP systems. In fact, early studies reported that the increased OXT and AVP mRNA and protein levels in the hypothalamic nuclei of the rat and prairie vole during the first 3 weeks after birth are critical (Almazan et al., 1989; Choy and Watkins, 1979; Lipari et al., 2001; Whitnall et al., 1985). A change in the biosynthesis form of OXT and changes in electrophysiological properties have also been reported during the early postnatal period (Grinevich et al., 2014). Likewise, OXT/AVP receptor mRNA expression peaks in cortical regions during the second postnatal week (Hammock and Levitt, 2013; Mitre et al., 2016; Newmaster et al., 2020; Vaidyanathan and Hammock, 2017). Although it is noteworthy that OXT and AVP receptors

[1]iMIND, Center of Excellence for Autism, le Vinatier Hospital, Bron, France

[2]Institute of Cognitive Science Marc Jeannerod, CNRS, Bron, France

[3]These authors contributed equally

[4]Lead contact

*Correspondence: angela.sirigu@isc.cnrs.fr

https://doi.org/10.1016/j.isci.2021.103655

expression can vary by species, sex, age, and social experiences (Albers, 2015; Smith et al., 2019), it is still largely unknown whether OXT and AVP neurons also exhibit a plastic distribution during early postnatal development. A very limited number of papers have addressed this question in rodents by counting the number of OXT or AVP immunoreactive (Ir) cells at different periods of time in voles at P1, P8, P21 (Yamamoto et al., 2004) and at P2, P9 (Kelly et al., 2018); in rats at P36 (DiBenedictis et al., 2017); and in mice at P5 (Godefroy et al., 2017) and at P0, P7 (Madrigal and Jurado, 2021). Although these previous findings indicate that OXT or AVP cells present distinct postnatal developmental dynamics, too few studies address the question of whether cells co-expressing OXT and AVP also exhibit a unique distribution by region and by age stage. In this study, we used 3D imaging of double immunolabeled cleared entire brains at different stages of early postnatal development to quantitatively map the spatio-temporal dynamics of OXT- and AVP-expressing cells in mice. We used C57BL/6J mice, because this strain is widely used as a model to understand the impact of OXT and AVP on social behavior. We examined whether OXT and AVP cells show spatial changes at early postnatal stages, i.e., birth (postnatal day 0, noted as P0), postnatal days P3, P7, and P14, through early adulthood ($\geq$P56), to cover developmental stages that represent the main neural growth events and behavioral milestones (Roubertoux et al., 2018; Todrank et al., 2005). At birth, mice pups are naive to any social experiences, and at P3, eyes/ear opening and independent locomotion have not yet occurred (Roubertoux et al., 2018). At P7, pups exhibit independent locomotion, and at P14, eyes are fully opened and the mice can function independently. In addition, for the first time, we co-registered the 3D images within the Allen Common Coordinate framework (Sunkin et al., 2012) to create an unbiased developmental atlas where we computed single-cell modeling (analysis of co-distribution, densities, and fluorescence intensity levels).

Our results show that the number of OXT cells selectively increases in different hypothalamic regions, in the periventricular preoptic nucleus (PvPO) and paraventricular nucleus (PVN), as well as in a novel atlas-based location that we named the antero-lateral preoptic area (ALPO). This expansion occurs during a critical window of postnatal development and with unique neural dynamics depending on the brain region. Because we analyzed a shorter time point during the first postnatal week at P3, we were able to show the co-existence of distinct dynamics within the OXT cell population. Of note, in the ALPO, the increase in OXT cell number starts immediately after birth to reach its final expression at P7, whereas in the PvPO and PVN, cell increase is delayed and begins 3 days after birth to progress until day 14, when an adult-like pattern is achieved. These results suggest that the ALPO- and PvPO/PVN-OXT neurons exhibit distinct cellular properties during unique critical periods of postnatal development, allowing upregulation of the peptide production and release on a much shorter timescale than has been previously observed. In addition, our 3D cell mapping analysis in the PVN provides further evidence of a cell-specific, age-specific, and region-specific pattern. We demonstrate a selective expansion of OXT cell number in the antero-ventral division of the PVN, whereas the postero-dorsal division contains cells present at birth. Interesting, although the number of OXT cells remains constant in this division, single cell analysis revealed that they exhibit a reduction of fluorescence intensity levels over time, suggesting the existence of distinct plastic mechanisms in the development of the PVN. Finally, we confirm the separate fate between OXT and AVP neural networks that are probably devoted to differently influence social brain functioning as physiological and behavioral development progresses. Together, our study presents the anatomical bases to understand the functional ontogeny of OXT and AVP neurons and strengthens the importance of the very early perinatal period in brain development.

RESULTS

Distinct OXT and AVP cell expression in the developing and adult mice brains

In a whole-brain approach using iDISCO+ (Renier et al., 2014), we employed double immunofluorescence labeling against OXT and AVP to detect the development of sub-population of cells co-expressing both peptides (Figures 1A and S5). Using hypothalamic 3D light sheet imaging, we first examined whether the total number of cells expressing OXT or AVP differs from birth until adulthood (Figure 1A; Video S1). Semi-automated cell counting (detailed in STAR Methods; example in Figure S6, Video S2) revealed considerable changes between the OXT and AVP cells dynamic across development (Figures 1B and 1C). At P0 and P3, brains contain similar numbers of OXT-immunoreactive (Ir) cells (P0: 1,556 $\pm$ 96 cells; P3: 1,901 $\pm$ 227 cells). However, from P3, the total number of OXT-Ir cells significantly increases by about 50% until adulthood ($F[4,19] = 107.1$, $p < 0.0001$; P56: 3,266 $\pm$ 191 cells). This increase is delayed and starts at P3, as no statistical difference was observed between P0 and P3 (mean diff -244.7; SE of diff 116.9; $p = 0.563$). This overall increase followed a dual pattern, with the first peak of $\sim$30% increase observed at P7

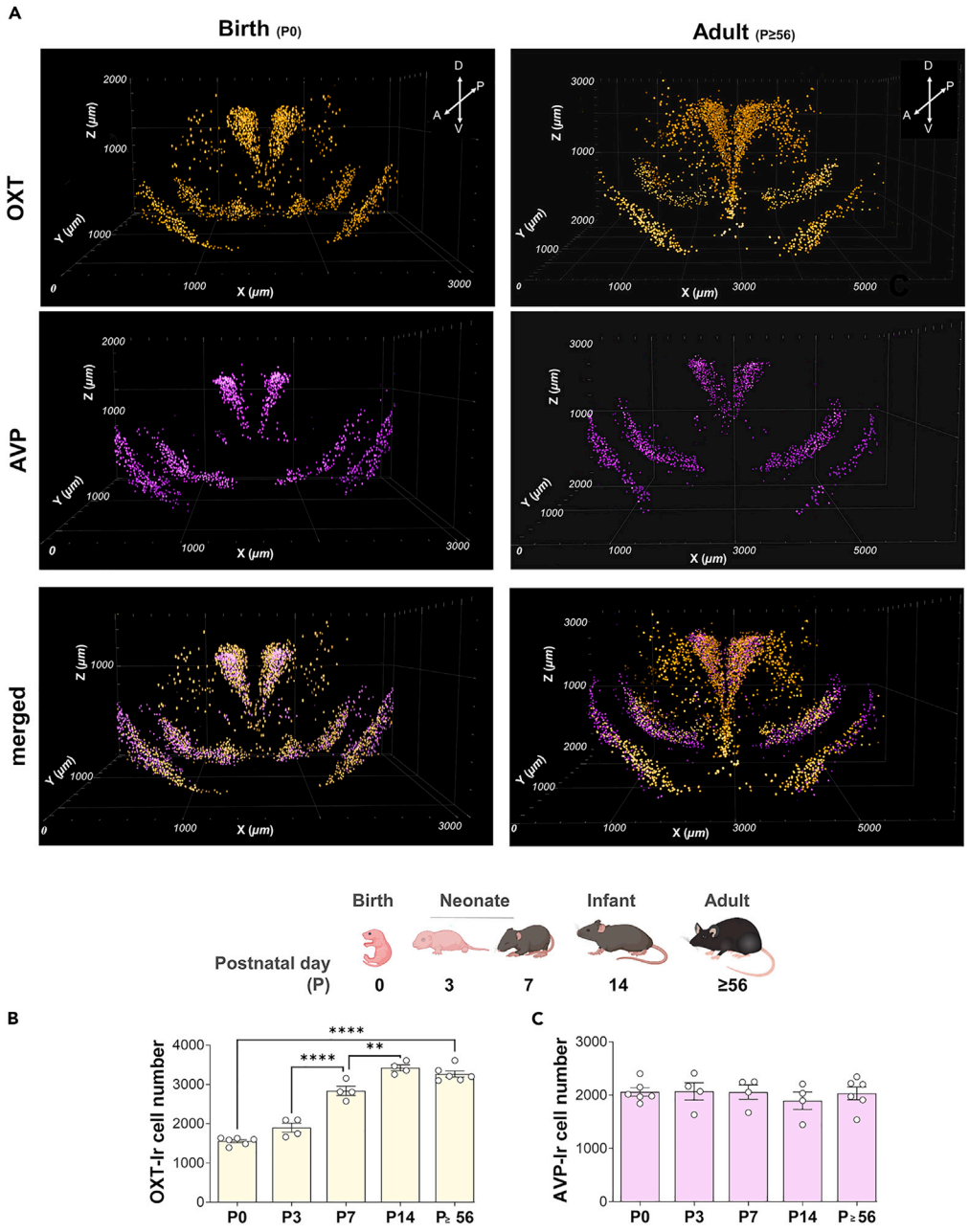

Figure 1. OXT and AVP cell expression in the developing and adult mice brains

(A) Three-dimensional visualization of brain OXT (pseudo-colored gold dots) and AVP (pseudo-colored purple dots) neurons at birth (P0; left panel) and in adulthood (P ≥ 56). Representative flat images show volumetric (x-y-z-) positions of the immunoreactive cell bodies, pictured as dots using the Imaris tool spot detection module, in the coronal plane. Images are obtained from 817 tiff images (thickness of 1,634 μm).

(B and C) (B) Brain OXT-Ir and (C) AVP-Ir cell number across development P0; P3, P7; P14 and P ≥ 56; n = 4–6 mice per age; ****P < 0.0001 between the P3 and P ≥ 56 groups, ****P <0.0001 between the P3 and P7 groups; **P < 0.01 between the P7 and P14 groups using one-way analysis of variance (ANOVA followed by Tukey's multiple-comparison test). Data are presented as mean ± SEM.

(mean diff P3 versus P7 -936.5; SE of diff 128.1; p <0.0001, P7: 2837 ± 239 cells), followed by the second increase of ~20% at P14 (mean diff P7 versus P14–585.3; SE of diff 128.1, p = 0.0017, P14: 3,422 ± 150 cells). The lack of additional changes between P14 and P56 (mean diff 156.8, SE of diff 116.9, p = 0.6704) suggests that the adult-like network pattern is achieved within the first 2 weeks of life in mice. By contrast, the total

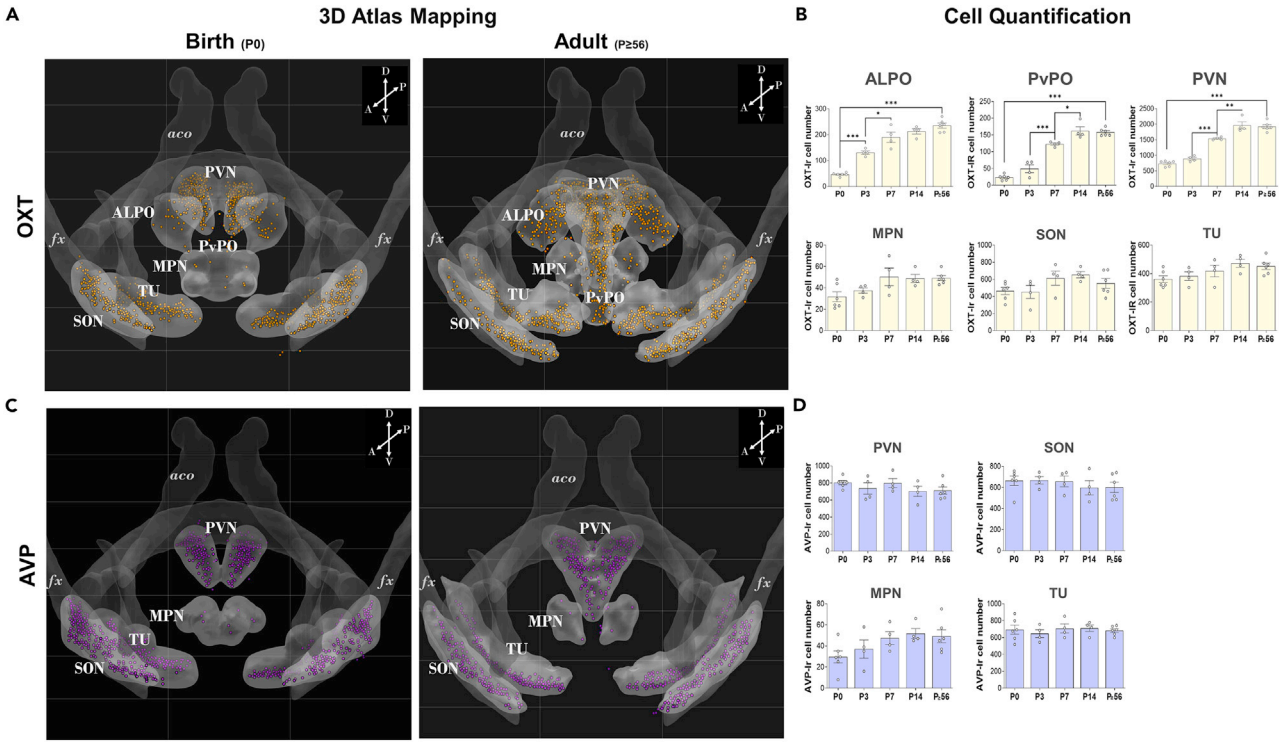

Figure 2. Spatiotemporal organization of OXT and AVP cells in the developing and adult hypothalamus

(A) Representative maps of the hypothalamic OXT-Ir cells, represented as gold dots, and aligned into the Allen Brain atlas. Annotated regions are displayed as light gray volumes, at birth (P0; left panel) and in adulthood (P ≥56); coronal plane. At birth, the 3D cellular maps (n = 3 animals) were fitted in the adult reference space (n = 6 animals) for direct comparison.

(B) Detailed quantitative analysis of the OXT-Ir in the PVN, PvPO, ALPO, MPN, SON, and TU across ages, denote unique sensitive periods of development for each brain region. n = 4–6 mice per age; *P <0.05; **P <0.01; ***P <0.001 between groups using one-way analysis of variance (ANOVA followed by Tukey's multiple-comparison test). Data are presented as mean ± SEM; ns, comparisons not significant (p >0.05).

(C) Representative maps of the hypothalamic AVP-Ir cells, represented as purple dots, and aligned into the Allen Brain atlas.

(D) Detailed quantitative analysis of the AVP-Ir in the PVN, SON, MPN, and TU across ages. Scale bars, 100 μm. Regions and fibers: PVN, paraventricular nucleus; PvPO, periventricular preoptic nucleus; ALPO, antero-lateral preoptic nucleus; SON, supraoptic nucleus; MPN, medial preoptic nucleus, which includes accessory magnocellular nuclei, such as the anterior hypothalamic area, circular nucleus, and preoptic area; TU, tuberal nucleus; ADP, antero-dorsal preoptic nucleus; PS, para-striatal nucleus; PD, postero-dorsal preoptic nucleus; and aco, anterior commissure; fx, fornix. Anatomical axes: D, dorsal; V, ventral; A, anterior; P, posterior.

number of AVP-Ir cells showed absolutely no difference at any age (F[4,19] = 0.2816, p = 0.8862; Figure 2C; P0: 2,060 ± 80 cells; P3: 2,070 ± 163 cells; P7: 2,056 ± 135 cells; P14: 1,895 ± 163 cells; P56: 2,032 ± 118 cells). Because the total number of cells expressing the mature form of AVP is identical to the number of cells expressing AVP-associated Neurophysin II form, at P0 and in adult mice (Figure S3), it is unlikely that the lack of developmental differences in the AVP cell number is due to a general change in the neurophysin expression across postnatal ages. The primary antibodies targeting the mature form of oxytocin (rabbit anti-OXT, Phoenix Pharma Inc, France, cat# G-051-01, 1:400) and the AVP-specific neurophysin II (mouse anti-AVP-NPII, Merck Millipore, Germany, cat# MABN845, clone PS41; 1:500) were used in combination. In our experimental condition, co-expression of OXT and AVP in the same cells is rare (≤1%) and was only found in paraventricular (PVN), supraoptic (SON), and tuberal (TU) nuclei of the hypothalamus (Figure S1), consistently with what has been previously described in adult mice with other primary antibodies simultaneous immunolabeling (Otero-García et al., 2016) and in agreement with the genetic molecular expression of OXT and AVP (Romanov et al., 2017, 2020). This pattern of labeling in which OXT and AVP cells mainly consist of single expression is also observed at the different developmental stages (Figure S2). Here, we used AVP-NPII-immunofluorescence labeling as a marker for the AVP neuronal population, as AVP-associated Neurophysin II and mature AVP are co-expressed by the same cells (Figure S3), as it was previously described in another experimental condition (Ben-Barak et al., 1985; Castel and Morris, 1988; Kawakami et al., 2021). Separate quantitative analysis also revealed a similar number of cells

immunoreactive for either AVP or AVP-NPII in the hypothalamus at birth and in the adult (Figure S3). Of interest, the reverse primary antibodies combination using the OXT-specific neurophysin I antibody (mouse anti-OXT-NPI, Merck Millipore, Germany, cat# MABN845, clone PS38; 1:500) with the mature form of AVP (rabbit anti-AVP, Phoenix Pharmaceutical, France, cat# G-065-07, 1:400) shows a similar pattern of expression as it is illustrated in the adult PVN, SON, and TU (Figure S4). These results indicate that, in C57BL6/J mice, the majority of the OXT- and AVP- expressing cells are immunoreactive for either OXT or AVP regardless of the developmental stage.

3D atlas-based mapping revealed distinct OXT and AVP dynamics in the hypothalamic nuclei

When considering the spatial localization of cells, adjacent Nissl-stain sections or equivalents are classically used as reference landmarks for visualization and to facilitate comparison of atlas annotation. However, this approach can lead to inaccurate anatomical maps. Here, we took advantage of the 3D approach to create an unbiased 3D atlas of the OXT and AVP cell population for the first time. Briefly, to generate a common annotated anatomical space during development and adulthood, each acquisition was re-referenced according to Allen's volumetric brain atlas (Wang et al., 2020) (see STAR Methods for details). Comparison of the 3D atlas maps revealed additional anatomical differences in the distribution of OXT and AVP neural networks across development (Figure 2A and Video S3). The majority of OXT-Ir and AVP-Ir cells (represented by pseudo-colored dots in the flat maps) are located in the hypothalamic PVN, and the supraoptic nucleus (SON), confirming the classical distribution in rodents. We also reported cell expression throughout the antero-posterior extent of the hypothalamus, in the medial preoptic nucleus (MPN) and periventricular preoptic (PvPO) area, as well as in the tuberal (TU) region. In our atlas-based classification, the medial preoptic nucleus corresponding to the previously described accessory magnocellular nuclei, including the anterior hypothalamic area, the circular nucleus, and the preoptic area, contains scattered OXT- and AVP-Ir cells (Møller et al., 2018; Rhodes et al., 1981). A specific group of OXT-Ir cells was identified in the antero-lateral part of the preoptic (ALPO) region (Figure 3). The integration of the x,y,z coordinate of each cell in the Allen Brain Atlas provided an accurate assessment of the position of this group of cells, as well as a multiplane registration. According to Allen Brain Atlas annotation, the boundaries of this OXT cell group are located in the preoptic area below the anterior commissure and are surrounded by the antero-dorsal preoptic (ADP), the para-striatal (PS) and the postero-dorsal preoptic (PD) nuclei (Figure 3). Double labeling revealed that this OXT cell cluster does not contain AVP-Ir cells (with AVP or AVP-NPII labeling), indicating that ALPO is a unique nucleus in the OXT/AVP network balance, which can be clearly distinguished from the BNST and the PVN despite its proximity to these regions. OXT and AVP-Ir cells are also present in extra-hypothalamic regions including the bed nucleus of stria terminalis (BNST) and the medial part of the amygdala (MEA) (Figure S7), as classically described.

In Figure 2, detailed quantitative analysis revealed that the numbers of OXT-Ir cells specifically increase in three brain regions, in the PVN ($F[4,19] = 94.43$, $p < 0.0001$), PvPO ($F[4,19] = 88.13$, $p < 0.0001$), and ALPO nuclei ($F[4,19] = 64.21$, $p < 0.0001$), but with unique developmental dynamics. In the ALPO, the numbers of OXT-Ir cells peaks at P3 and P7 (mean diff P0 versus P3 -84.42; SE of diff 14.52; $p = 0.0001$; mean diff P3 versus P7 -59.75; SE of diff 15.90; $p = 0.0103$; mean diff P7 versus P14–22.5; SE of diff 15.9; $p = 0.6262$; mean diff P14 versus P $\geq$56 22.33; SE of diff 14.52; $p = 0.5518$; Figure 2B). However, in the PVN, the number of cells expressing OXT increased from P3 to P14 (Figure 2B), with two peaks at P7 and P14 (mean diff P0 versus P3 -151.3; SE of diff 85.78; $p = 0.422$; mean diff P3 versus P7 -649; SE of diff 93.97; $p < 0.0001$; mean diff P7 versus P14 –422.5; SE of diff 93.97; $p = 0.002$; mean diff P14 versus P $\geq$56 34.25; SE of diff 85.78; $p = 0.9942$). A similar pattern was observed in the PvPO (mean diff P0 versus P3 -26.25; SE of diff 9.93; $p = 0.1018$; mean diff P3 versus P7 -73.5; SE of diff 10.88; $p < 0.0001$; mean diff P7 versus P14–39.25; SE of diff 10.88; $p = 0.0143$; mean diff P14 versus P $\geq$56 4.0; SE of diff 9.33; $p = 0.994$). In the other hypothalamic regions, including the SON, TU, and MPN, no changes across development were detected (SON ($F[4,19] = 2.103$, $p = 0.1203$), TU ($F[4,19] = 2.737$, $p = 0.0694$), MPN ($F[4,19] = 2.373$, $p = 0.0899$); Figure 2B). In these hypothalamic regions, the total number of AVP-Ir cells show absolutely no change regardless of age (PVN ($F[4,19] = 1.075$, $p = 0.3965$); SON ($F[4,19] = 0.4924$, $p = 0.7414$), TU ($F[4,19] = 0.2743$, $p = 0.8909$), MPN ($F[4,19] = 2.332$, $p = 0.0929$); Figure 2B). In addition, the number of AVP cells present in the BNST and MEA did not change across ages (Figure S7).

Onset of OXT cell expansion and AVP reorganization in the PVN

Given the unique temporal dynamics of OXT and AVP cells populating the PVN, we next investigated whether specific spatial arrangement patterns occur between the two populations over the course of development

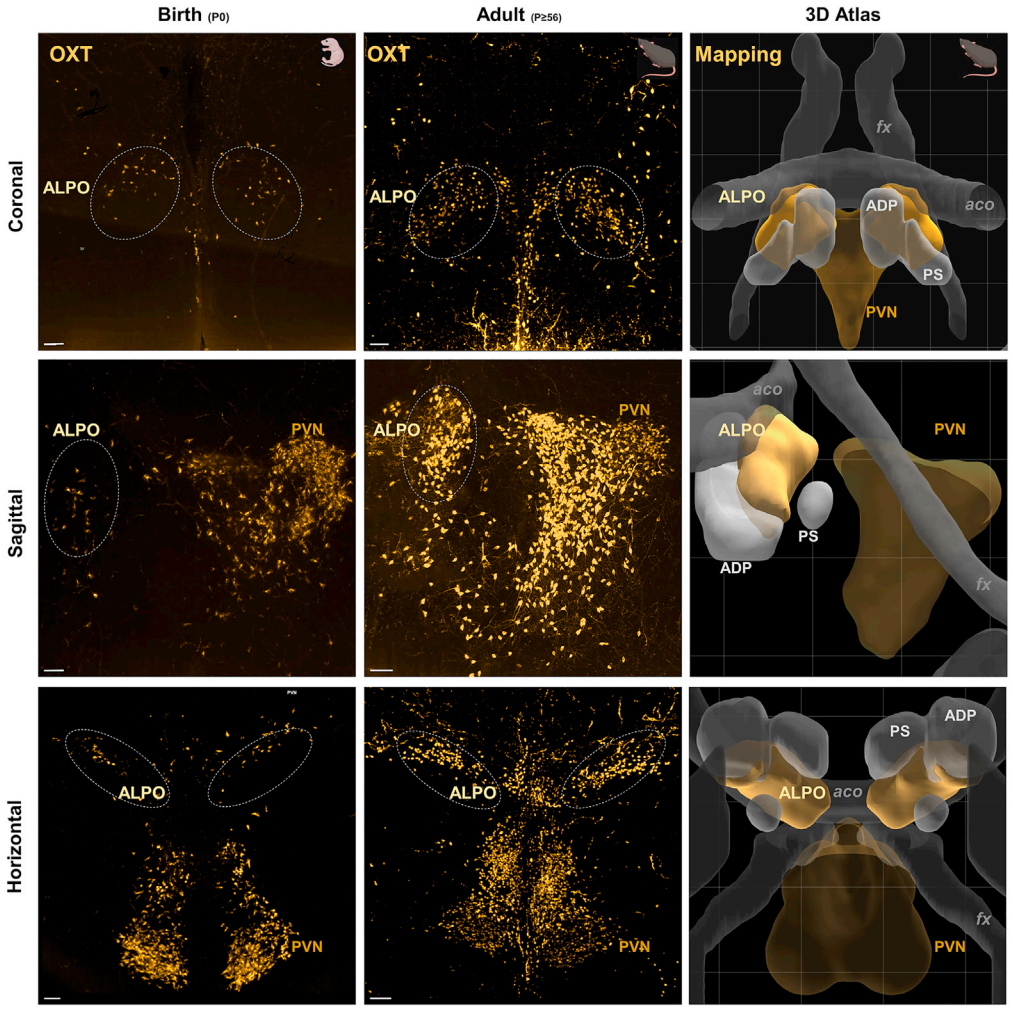

Figure 3. Immunofluorescence labeling of OXT cells in the ALPO

Images of the OXT immunofluorescence labeling in the ALPO and PVN nuclei at birth (P0; left column) and in adulthood (P >56; middle column) are shown in coronal (top), sagittal (middle), and horizontal (bottom) planes. 3D mapping of the ALPO nucleus: corresponding registered OXT cell volumes (light gold) are shown. Scale bars, 100 μm. Regions and fibers: ALPO, antero-lateral preoptic nucleus; PVN, paraventricular nucleus; ADP, antero-dorsal preoptic nucleus; PS, para-striatal nucleus; and aco, anterior commissure; fx, fornix.

(Figures 4 and S8; Video S4). Multiplane views of immunofluorescence labeling show that OXT-Ir and AVP-Ir cells are distributed differently, forming a separated pattern at birth compared with adulthood (Figure 4A). To model this neuro-anatomical organization, we plotted and color-coded the OXT and AVP x,y,z cell positions for all animals (P0, P3 P7, P14: n = 3 mice for each age group; P ≥ 56 n = 6 mice). However, for a better display, a virtual animal obtained by sub-sampling, the set of cells detected for each age group is processed to be illustrated in coronal, horizontal, and sagittal planes (Figure 4B). As a result, we show that OXT and AVP cells occupy two distinct regions in early development but not in adulthood. At P0, OXT and AVP cells are mostly distributed away from each other, forming two distinct non-overlapping but contiguous clusters along the same anatomical axis (Figure 4B), although some OXT cells are also located where AVP cells reside. In this innate/congenital configuration, the majority of OXT cells populate the posterior part of the PVN (shown in the horizontal and sagittal planes), at the dorsal level (coronal plane). This parcellation is maintained at P3, yet, from this time, additional OXT neurons are progressively found in the anterior part, and in the ventral domain along the third ventricle, where AVP cells natively reside, forming overlapping cell groups by P7. Additional 3D representations of the molecular volume occupied by OXT and AVP cells in the PVN (Figure 4C) further illustrate the progressive shift in OXT networks occupancy from 50% to 70% of the PVN volume.

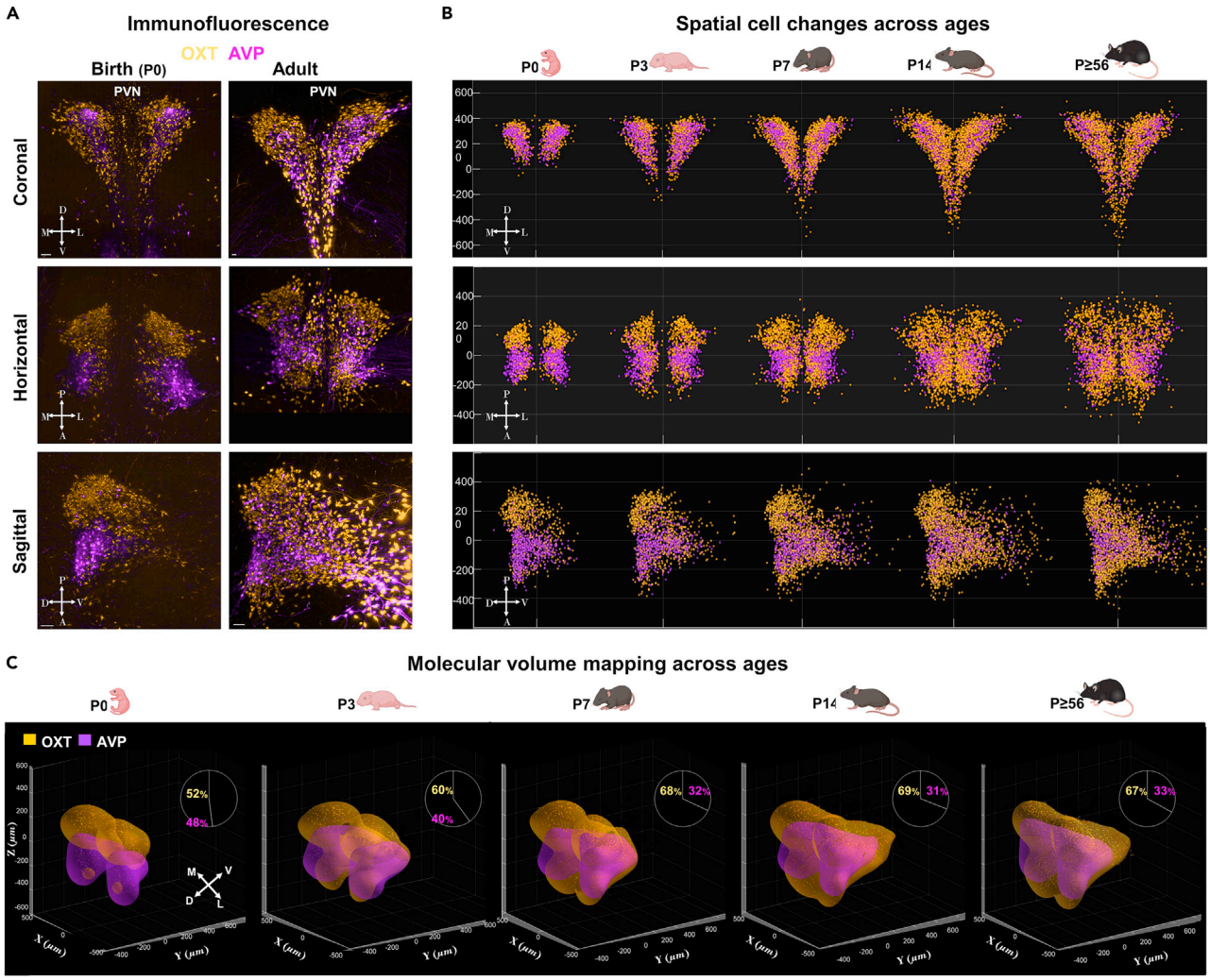

Figure 4. OXT cell expansion and AVP reorganization cells in the paraventricular nucleus

(A) Double immunofluorescence labeling of OXT- (gold) and AVP-Ir cells (magenta) in the PVN, at birth (PO; left) and in adulthood (P56; right). Coronal (top), horizontal (middle), and sagittal (bottom) planes are displayed. Scale bars, 100 μm.

(B) 3D plotting and flat mapping summarizing average Cartesian coordinates (in μm) of the OXT (gold dots) and AVP (magenta dots) neurons for each age group ($n = 3$ mice at P0, P3, P7, P14; $n = 6$ mice at P ≥ 56). Coronal (top), horizontal (middle), and sagittal (bottom) views illustrate the specific spatiotemporal arrangements of OXT- and AVP-PVN networks.

(C) 3D representation of the molecular volume occupied by OXT cells (yellow dots in yellow volume) and AVP cells (magenta dots in magenta volume) across development. The ratio between OXT and AVP volume occupancy, expressed as percentage of the total PVN is included on the side for each age group.

Density- and staining intensity-based analyses revealed OXT-PVN clusters dynamic

To decipher the spatial-micro-organization of OXT neurons in the PVN, we next used a nearest neighbor detection algorithm to estimate local densities (Figures 5 and S8F). This density-based analysis maps the PVN into areas from the lowest to the highest densities (blue, <60 cells/μm^3; yellow, >100 cells/μm^3; Figure 5A). As a result, we dissociated the PVN into two developmental clusters according to the density dynamics of the OXT cells. In all age groups, clusters of high densities are found in the posterior sector. However, at P7, a stable peak in density appears in the anterior region along the dorsoventral axis of the PVN, as illustrated in the coronal (top) and sagittal views (bottom) in Figure 5B. Therefore, the ontogenetic changes of PVN are selective to a cluster of OXT cells located in the antero-posterior area. Quantitative analysis further indicates that a specific growth appears at P7 in the anterior cluster, while the number of OXT-Ir cells present in the posterior cluster remains stable over time (Figure 5B). In striking contrast, AVP-cell-density based processing does not show such developmental micro-organization (data not illustrated).

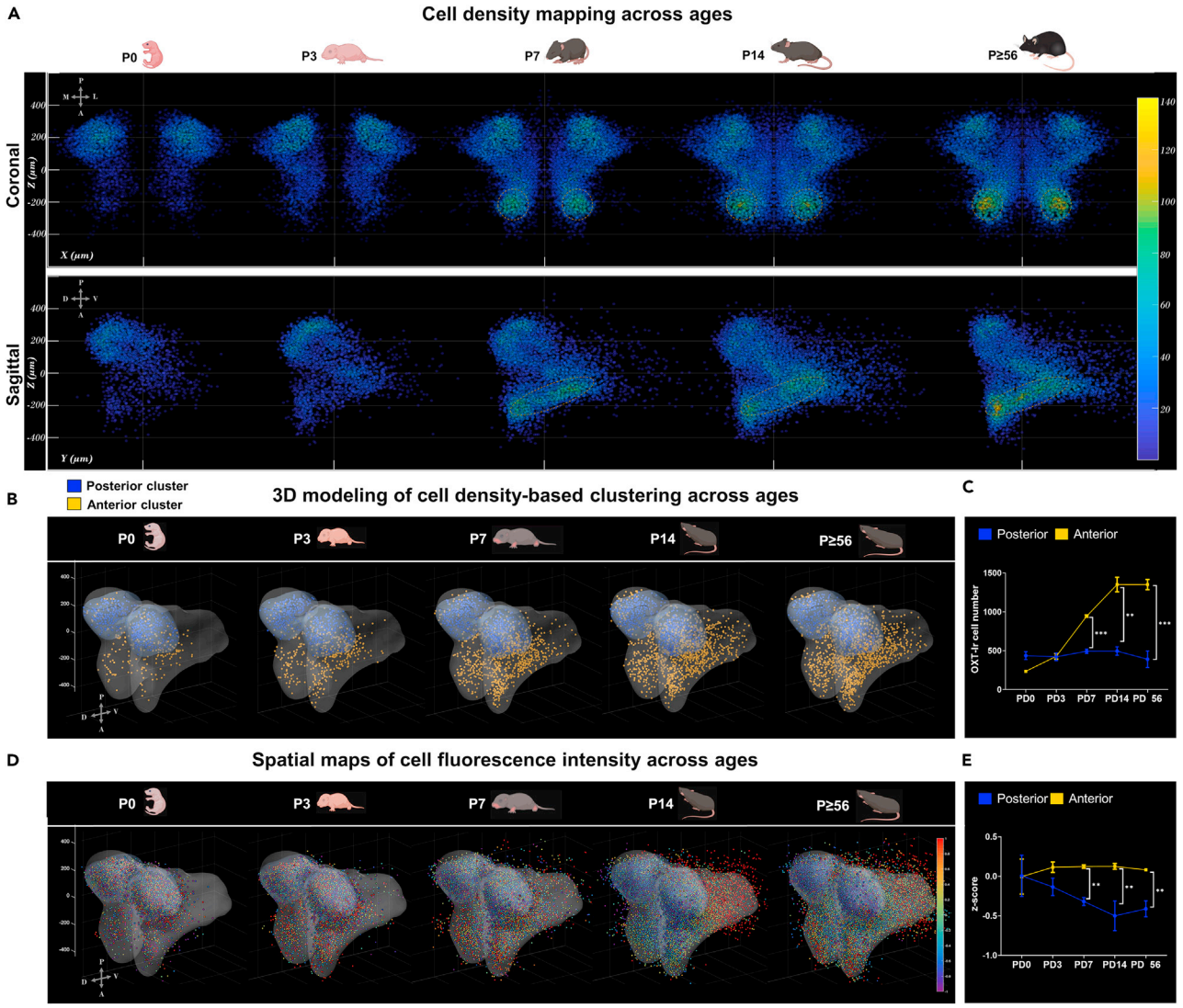

Figure 5. Developmental changes of OXT cells along the antero-posterior axis of the paraventricular nucleus

(A) Cell-based density distribution of OXT cells in the PVN across development. Sub-areas of high (yellow-orange; >100 cells/μm^3), intermediate (green; 60–100 cells//μm^3), and low (blue; <60 cells/μm^3) densities are displayed in coronal (top) and sagittal (bottom) planes.

(B) 3D modeling illustrating the antero-posterior clustering within the OXT cell population in the PVN across development.

(C) Cell quantification of OXT-Ir cells located in the anterior and posterior clusters.

(D) 3D representation of the animal-based z-transformed fluorescence intensity level for each OXT cell in the anterior (gray volume) and posterior (blue) clusters across development.

(E) Group analysis of the mean relative fluorescence in the anterior and posterior clusters.

We then used the distribution of fluorescence intensity as an indirect indicator of protein expression levels (Coffman and Wu, 2012; Verdaasdonk et al., 2014). For each identified cell, the fluorescence value was estimated based on the voxel maximum intensity (Imaris Software, Bitplane, Oxford Instrument). Because the fluorescence intensity levels are not directly comparable between separate acquisitions, each fluorescence value was systematically Z-transformed for each subject within the region of interest (Figures 5D and S8). As illustrated in the 3D representation, no particular spatial configuration is present at birth, although marked hypo-fluorescence signals appear in the posterior area as development progresses. Group analysis of the mean relative fluorescence in the anterior and posterior cluster confirms that, since P14, OXT cells present in the posterior cluster present significant hypo-fluorescence signals (Figure 5E), which may correlate with neurite formation and extension.

DISCUSSION

An unbiased 3D atlas mapping of the postnatal trajectories of OXT and AVP cells revealed unique anatomical properties of OXT and AVP neurons in neonatal mice and showed dramatic developmental differences between and within the two neural networks during very early development. We found that the number of OXT neurons doubles in selective hypothalamic regions, the ALPO, PvPO, and PVN, but with unique temporal dynamics. In the ALPO, which is a unique node in the OXT/AVP systems, containing only OXT-expressing cells and not AVP cells, the increase begins immediately after birth to reach its final expression by P7. In contrast, in PvPO and PVN, the increase is delayed and starts 3 days after birth until day 14, when an adult-like pattern is achieved. These results indicate that OXT cells present a different ontogenic origin. Further analysis of single-cell density in the PVN showed that OXT-expressing cells typically emerge in the antero-ventral division, whereas the number of OXT cells remains constant in the postero-dorsal division. We also found a decrease in fluorescence intensity levels of individual cells in the postero-dorsal division, suggesting typical functional properties as development proceeds. In contrast, AVP neurons do not undergo such a delay in maturation. Therefore, our results show selective tuning of OXT cells after birth suggesting that maturation of the OXT system requires social experience to fully develop.

We have shown that the overall number of AVP-expressing cells in the different hypothalamic nuclei (PVN, SON, MPN, TU), as well as in the extra-hypothalamic regions, MEA and BNST, remains stable over time, from birth to adulthood. However, because we have not quantified the number of AVP-expressing cells present in the suprachiasmatic (SCH) nucleus, we cannot rule out a developmental reorganization in this particular hypothalamic region, as has been recently shown (Madrigal and Jurado, 2021). A critical step for assessing the role of oxytocin and vasopressin on brain function is accurate enumeration and comparison of the number of OXT and AVP cells in the different brain regions at different developmental stages. However, there are very little available data covering this question, especially in mice. Previous results focused on a single postnatal time point (Godefroy et al., 2017; Song and Albers, 2018), whereas, to the extent of our knowledge, only one recent paper has examined the developmental co-dynamics of OXT and AVP cell numbers with different time windows (Madrigal and Jurado, 2021). Extrapolated numbers from this study (Madrigal and Jurado, 2021) report values of about 1,210 OXT cells at P0 and about 3,016 OXT cells at P7, whereas we report a total number of about 1,556 OXT cells at P0 and 2,837 at P7. By comparison, absolute numbers for OXT cells within each mouse line, ICR mice in Madrigal and Jurado (2021) and C57BL/6J in the present study, are similar, whereas the total numbers of AVP cells vary by a factor of almost 2, that is, 2,228 AVP cells at P0 and 4,069 at P7 in Madrigal and Jurado (2021), whereas we report 2,060 AVP cells at P0 and 2,056 at P7. In addition, another study performed at P5 in C57BL6J mice (Godefroy et al., 2017) revealed a total smaller number of 409 AVP cells, when 952 cells were found at P7 by Madrigal and Jurado (2021). By comparison with the same ICR strain used in Madrigal and Jurado (2021), a previous study reported about 1,300 AVP cells in the PVN versus 600 (Ison et al., 1993). Factors such as the primary antibodies used, the method of cell counting, and most importantly inappropriate light sheet parameters (see STAR Methods for details) could explain such differences in AVP cell expression between our data and those reported by Madrigal and Jurado (2021). Nevertheless, our results indicate that the AVP neural networks mature earlier than those of the OXT system, are present at birth, and remain stable over time. The lack of developmental partitioning in the AVP cell population supports the idea that the unique developmental dynamics of the OXT system is not just due to brain growth expansion

In our study, because we focused on early and late postnatal development (P0, P3, P7, P14), we were able to identify sub-windows critical for the OXT system. In the ALPO region, the increase in OXT cell numbers starts immediately at birth to reach its final expression by P7, whereas in the PvPO and PVN, the increase is delayed and begins 3 days after birth until day 14. As timing and temporal schemes during embryonic genesis relate to specification of distinct neuronal identities, it will be interesting to determine specific gene expression patterns of these OXT cell groups expressed in the ALPO and the PVN, and whether and how they related to distinct neural circuits.

In the PVN, several cellular and molecular mechanisms might explain this delayed maturation of the OXT cells. A likely candidate for the addition of new OXT-expressing neurons is the formation of new neurons. Indeed, adult neurogenesis has been reported in the hypothalamus in mice (Cheng, 2013) at the level of specific niches located in the wall of the third ventricle in the ventrolateral regions (Maggi et al., 2014; Yoo and Blackshaw, 2018). Noteworthy, cell proliferation can be increased in the adult PVN (Pencea

et al., 2001), indicating that this brain region retains neurogenic activity throughout life. Considering the periventricular location of the PvPO, similar mechanism could be involved in this nucleus. Alternatively, this delayed maturation may be associated with an up-regulation in the expression of the OXT protein in originally immunonegative cells. This process may be connected to the proper phenotypic expression of each neuron. In fact, single-cell RNA sequencing showed that OXT expression is mostly a postnatal event (Romanov et al., 2020). It can be argued that the interplay between internal and environmental signals promotes the expression of OXT in a pool of silent neurons but ready to express OXT, to up-regulate the buffering capacity of OXT to cope with environmental challenges (Quintana and Guastella, 2020). In this speculating scenario, changes in OXT cell numbers and signaling may reflect the physiological needs associated with the different stages of social development. Further studies will be needed to determine whether, during defined time windows, OXT neurons undergo experience-dependent survival and/or phenotypic expression.

By translating the three-dimensional coordinates of OXT and AVP cells into a customized brain atlas using the Allen Brain Atlas annotation, we were also able for the first time to circumscribe a group of OXT cells in a region we named the ALPO (antero-lateral preoptic) nucleus. This OXT cell group (lacking AVP cell expression) has also been identified in the extended ventral BSNT region in ICR mice (Madrigal and Jurado, 2021, based on Paxinos and Franklin atlas), in the anterior commissural nucleus and antero-dorsal preoptic nucleus in CD1 mice (Otero-García et al., 2016, based on Paxinos and Franklin atlas), and in the strio-hypothalamic nucleus in transgenic mouse line (Liao et al., 2020, based on Paxinos and Franklin atlas). The later expression of OXT cells in the anterior-ventral part of the PVN or in the ALPO nuclei suggests that these neurons are a critical node of neural pathways integrating signals from the outside world and may subserve in the development of social behavior. In fact, these "innate/congenital" and "acquired/adaptive" OXT cells may help to establish a behavioral switch in the animal's social needs, initiated by a closed parental bond (i.e., mother-pup) and progressing to more socially engaged interactions (i.e., peers/siblings). Although the OXT-PVN cells are likely to preferentially support these social features (Resendez et al., 2020; Veenema and Neumann, 2008), we cannot rule out the possibility that OXT-ALPO cells are additional components for the proper expression of social behavior. Indeed, the preoptic area regulates parental behavior in mice (Kuroda and Numan, 2014).

Finally, our immunofluorescence signal processing analysis in the PVN establishes the existence of two main OXT neural networks with potential innate/congenital and acquired/adaptive properties. The innate OXT networks present at birth and located in the postero-dorsal part where the parvo-cells are classically found could represent the initial/primary population of OXT neurons involved in the animal's first social experience such as bonding with the dam and siblings. In addition, we found that, from P7, this putative parvo-OXT cells group show hypo-fluorescence signaling. This suggests that, as cells mature, they release more OXT that is transported out of the cell body along the fibers to its final destination. This hypothesis is consistent with the increase in OXT levels in the cortex due to high PVN activity in the first postnatal week (Zheng et al., 2014). It has been shown that the density and staining intensity of oxytocinergic fibers markedly increases during the first few weeks of postnatal development (Grinevich et al., 2014). These developmental changes in the local and extra-hypothalamic projections might be particularly important for understanding the postnatal dynamics of neuropeptidergic modulation of socio-emotional behaviors. In our study we found this reduction in cell body fluorescence intensity in the later postnatal period (P14) compared with earlier postnatal ages (P0–P7) suggesting that these neurons do not have full projections into which to disperse the peptides produced in the early postnatal period and, therefore, they accumulate them in the cell bodies. However, it is unclear whether the observed postnatal decrease in immunolabeling in our study reflects increased delivery of OXT from hypothalamic perikarya to their distal axon segments or a reduction in OXT synthesis and production.

Together, our findings have potential implications for understanding how (OXT/AVP balance), where (region specificity), and when (temporal specificity) the neuronal circuits involved in social brain processing are established and reveal the unique ontogenic potential of OXT and AVP systems for the state and fate of prosocial brain properties.

Limitations of the study

In this study we focused on the organization of OXT and AVP cells and their postnatal functional expression. However, to understand how such organization is integrated into multiple hypothalamic and

extrahypothalamic networks it is necessary to focus on OXT and AVP projections, which was not addressed in this study. Although the light-sheet imaging approach has been optimized for capturing the intact rodents' brain, further development is still needed to efficiently quantify, map, and compare OCT and AVP projections density within the entire brain. Handling, detecting, and analyzing such large datasets would require methodological innovations, such as advanced automated detection algorithms based on deep learning technology, coupled with rigorous supervisions. The implementation of other strategies such as viral vector tracing approaches with cell type-specific reporter could help in this direction.

STAR★METHODS

Detailed methods are provided in the online version of this paper and include the following:

- KEY RESOURCES TABLE
- RESOURCE AVAILABILITY
  - Lead contact
  - Materials availability
  - Data and code availability
- EXPERIMENTAL MODEL AND SUBJECT DETAILS
- METHOD DETAILS
  - Intracardiac perfusion
  - Whole brain pre-processing and immunofluorescence labeling
  - Tissue clearing
  - Light-sheet microscopy imaging settings
- QUANTIFICATION AND STATISTICAL ANALYSIS
  - Cell detection, cell quantification and region identification
  - Mesoscopic analysis and image processing
  - Single-cell processing and 3D modeling
  - Statistical analysis

SUPPLEMENTAL INFORMATION

Supplemental information can be found online at https://doi.org/10.1016/j.isci.2021.103655.

ACKNOWLEDGMENTS

This research is funded by Centre National de la Recherche Scientifique, le Vinatier Hospital and ANR (16-CE37-0017-01, 17-CE37-0015-01), and a Labex Cortex (ANR-11–LABEX-0042) grant from the University of Lyon I in the program "Investissement d'Avenir." We thank the genotyping facility (SFR Biosciences-ENS Lyon) and the animal facility (iXplora-CarMen Laboratory U1060) for allowing access to the animal facilities. A special thanks to Olivier Raineteau for helpful discussion during data acquisition and to Bruno Pillot for help during animals' care.

AUTHOR CONTRIBUTIONS

Conceptualization: A. Sirigu; methodology: A. Soumier, M.H., G.L.; software: G.L.; validation: A. Soumier and M.H.; formal analysis: A. Soumier, M.H., G.L.; investigation: A. Soumier, M.H., G.L.; resources: A. Sirigu and C.D.; data curation: G.L.; writing - original draft: A. Soumier and A. Sirigu; writing - review & editing: A. Soumier, M.H., G.L., C.D., and A. Sirigu; visualization: A. Soumier, M.H., G.L.; supervision: A. Sirigu; project administration: A. Sirigu and C.D.; funding acquisition: A. Sirigu and C.D.

DECLARATION OF INTERESTS

The authors declare no competing interests.

Received: November 19, 2021
Revised: December 3, 2021
Accepted: December 14, 2021
Published: January 21, 2022

REFERENCES

Albers, H.E. (2015). Species, sex and individual differences in the vasotocin/vasopressin system: relationship to neurochemical signaling in the social behavior neural network. Front. Neuroendocrinol. *36*, 49–71. https://doi.org/10.1016/j.yfrne.2014.07.001.

Almazan, G., Lefebvre, D.L., and Zingg, H.H. (1989). Ontogeny of hypothalamic vasopressin, oxytocin and somatostatin gene expression. Brain Res. Dev. Brain Res. *45*, 69–75. https://doi.org/10.1016/0165-3806(89)90008-4.

Andari, E., Richard, N., Leboyer, M., and Sirigu, A. (2016). Adaptive coding of the value of social cues with oxytocin, an fMRI study in autism spectrum disorder. Cortex J. Devoted Study Nerv. Syst. Behav. *76*, 79–88. https://doi.org/10.1016/j.cortex.2015.12.010.

Andari, E., Schneider, F.C., Mottolese, R., Vindras, P., and Sirigu, A. (2014). Oxytocin's fingerprint in personality traits and regional brain volume. Cereb. Cortex. *24*, 479–486. https://doi.org/10.1093/cercor/bhs328.

Ben-Barak, Y., Russell, J.T., Whitnall, M.H., Ozato, K., and Gainer, H. (1985). Neurophysin in the hypothalamo-neurohypophysial system. I. Production and characterization of monoclonal antibodies. J. Neurosci. *5*, 81–97.

Carter, C.S. (2017). The oxytocin-vasopressin pathway in the context of love and fear. Front. Endocrinol. *8*, 356. https://doi.org/10.3389/fendo.2017.00356.

Castel, M., and Morris, J.F. (1988). The neurophysin-containing innervation of the forebrain of the mouse. Neuroscience *24*, 937–966. https://doi.org/10.1016/0306-4522(88)90078-4.

Cheng, M.-F. (2013). Hypothalamic neurogenesis in the adult brain. Front. Neuroendocrinol. *34*, 167–178. https://doi.org/10.1016/j.yfrne.2013.05.001.

Choy, V.J., and Watkins, W.B. (1979). Maturation of the hypothalamo-neurohypophysial system. I. Localization of neurophysin, oxytocin and vasopressin in the hypothalamus and neural lobe of the developing rat brain. Cell Tissue Res. *197*, 325–336. https://doi.org/10.1007/BF00233923.

Coffman, V.C., and Wu, J.-Q. (2012). Counting protein molecules using quantitative fluorescence microscopy. Trends Biochem. Sci. *37*, 499–506. https://doi.org/10.1016/j.tibs.2012.08.002.

Curley, J.P., and Champagne, F.A. (2016). Influence of maternal care on the developing brain: mechanisms, temporal dynamics and sensitive periods. Front. Neuroendocrinol. *40*, 52–66. https://doi.org/10.1016/j.yfrne.2015.11.001.

DiBenedictis, B.T., Nussbaum, E.R., Cheung, H.K., and Veenema, A.H. (2017). Quantitative mapping reveals age and sex differences in vasopressin, but not oxytocin, immunoreactivity in the rat social behavior neural network. J. Comp. Neurol. *525*, 2549–2570. https://doi.org/10.1002/cne.24216.

Donaldson, Z.R., and Young, L.J. (2008). Oxytocin, vasopressin, and the neurogenetics of sociality. Science *322*, 900–904. https://doi.org/10.1126/science.1158668.

Dumais, K.M., and Veenema, A.H. (2016). Vasopressin and oxytocin receptor systems in the brain: sex differences and sex-specific regulation of social behavior. Front. Neuroendocrinol. *40*, 1–23. https://doi.org/10.1016/j.yfrne.2015.04.003.

Enes-Marques, S., and Giusti-Paiva, A. (2018). Litter size reduction accentuates maternal care and alters behavioral and physiological phenotypes in rat adult offspring. J. Physiol. Sci. *68*, 789–798. https://doi.org/10.1007/s12576-018-0594-8.

Franks, B., Champagne, F.A., and Curley, J.P. (2015). Postnatal maternal care predicts divergent weaning strategies and the development of social behavior. Dev. Psychobiol. *57*, 809–817. https://doi.org/10.1002/dev.21326.

Godefroy, D., Dominici, C., Hardin-Pouzet, H., Anouar, Y., Melik-Parsadaniantz, S., Rostène, W., and Reaux-Le Goazigo, A. (2017). Three-dimensional distribution of tyrosine hydroxylase, vasopressin and oxytocin neurones in the transparent postnatal mouse brain. J. Neuroendocrinol. *29*. https://doi.org/10.1111/jne.12551.

Grinevich, V., Desarménien, M.G., Chini, B., Tauber, M., and Muscatelli, F. (2014). Ontogenesis of oxytocin pathways in the mammalian brain: late maturation and psychosocial disorders. Front. Neuroanat. *8*, 164. https://doi.org/10.3389/fnana.2014.00164.

Grinevich, V., and Neumann, I.D. (2021). Brain oxytocin: how puzzle stones from animal studies translate into psychiatry. Mol. Psychiatry *26*, 265–279. https://doi.org/10.1038/s41380-020-0802-9.

Hammock, E.A.D., and Levitt, P. (2013). Oxytocin receptor ligand binding in embryonic tissue and postnatal brain development of the C57BL/6J mouse. Front. Behav. Neurosci. *7*, 195. https://doi.org/10.3389/fnbeh.2013.00195.

Ison, A., Yuri, K., Ueta, Y., Leng, G., Koizumi, K., Yamashita, H., and Kawata, M. (1993). Vasopressin- and oxytocin-immunoreactive hypothalamic neurones of inbred polydipsic mice. Brain Res. Bull. *31*, 405–414. https://doi.org/10.1016/0361-9230(93)90234-3.

Johnson, Z.V., and Young, L.J. (2017). Oxytocin and vasopressin neural networks: implications for social behavioral diversity and translational neuroscience. Neurosci. Biobehav. Rev. *76*, 87–98. https://doi.org/10.1016/j.neubiorev.2017.01.034.

Kawakami, N., Otubo, A., Maejima, S., Talukder, A.H., Satoh, K., Oti, T., Takanami, K., Ueda, Y., Itoi, K., Morris, J.F., et al. (2021). Variation of pro-vasopressin processing in parvocellular and magnocellular neurons in the paraventricular nucleus of the hypothalamus: evidence from the vasopressin-related glycopeptide copeptin. J. Comp. Neurol. *529*, 1372–1390. https://doi.org/10.1002/cne.25026.

Kelly, A.M., Hiura, L.C., and Ophir, A.G. (2018). Rapid nonapeptide synthesis during a critical period of development in the prairie vole: plasticity of the paraventricular nucleus of the hypothalamus. Brain Struct. Funct. *223*, 2547–2560. https://doi.org/10.1007/s00429-018-1640-2.

Kuroda, K.O., and Numan, M. (2014). The medial preoptic area and the regulation of parental behavior. Neurosci. Bull. *30*, 863–865. https://doi.org/10.1007/s12264-014-1462-z.

Lefevre, A., and Sirigu, A. (2016). The two fold role of oxytocin in social developmental disorders: a cause and a remedy? Neurosci. Biobehav. Rev. *63*, 168–176. https://doi.org/10.1016/j.neubiorev.2016.01.011.

Liao, P.-Y., Chiu, Y.-M., Yu, J.-H., and Chen, S.-K. (2020). Mapping central projection of oxytocin neurons in unmated mice using cre and alkaline phosphatase reporter. Front. Neuroanat. *14*, 559402. https://doi.org/10.3389/fnana.2020.559402.

Lipari, E.F., Lipari, D., Gerbino, A., Di Liberto, D., Bellafiore, M., Catalano, M., and Valentino, B. (2001). The hypothalamic magnocellular neurosecretory system in developing rats. Eur. J. Histochem. *45*, 163–168. https://doi.org/10.4081/1626.

Madrigal, M.P., and Jurado, S. (2021). Specification of oxytocinergic and vasopressinergic circuits in the developing mouse brain. Commun. Biol. *4*, 586. https://doi.org/10.1038/s42003-021-02110-4.

Maggi, R., Zasso, J., and Conti, L. (2014). Neurodevelopmental origin and adult neurogenesis of the neuroendocrine hypothalamus. Front. Cell. Neurosci. *8*, 440. https://doi.org/10.3389/fncel.2014.00440.

Mitre, M., Marlin, B.J., Schiavo, J.K., Morina, E., Norden, S.E., Hackett, T.A., Aoki, C.J., Chao, M.V., and Froemke, R.C. (2016). A distributed network for social cognition enriched for oxytocin receptors. J. Neurosci. *36*, 2517–2535. https://doi.org/10.1523/JNEUROSCI.2409-15.2016.

Møller, M., Busch, J.R., Jacobsen, C., Lundemose, S.B., Lynnerup, N., Rath, M.F., and Banner, J. (2018). The accessory magnocellular neurosecretory system of the rostral human hypothalamus. Cell Tissue Res. *373*, 487–498. https://doi.org/10.1007/s00441-018-2818-x.

Morikawa, T., Yamamoto, Y., and Miyaishi, S. (2011). A new method for sex determination based on detection of SRY, STS and amelogenin gene regions with simultaneous amplification of their homologous sequences by a multiplex PCR. Acta Med. Okayama *65*, 113–122. https://doi.org/10.18926/AMO/45270.

Myronenko, A., and Song, X. (2010). Point set registration: coherent point drift. IEEE Trans. Pattern Anal. Mach. Intell. *32*, 2262–2275. https://doi.org/10.1109/TPAMI.2010.46.

Newmaster, K.T., Nolan, Z.T., Chon, U., Vanselow, D.J., Weit, A.R., Tabbaa, M., Hidema, S., Nishimori, K., Hammock, E.A.D., and Kim, Y. (2020). Quantitative cellular-resolution map of the oxytocin receptor in postnatally developing

mouse brains. Nat. Commun. *11*, 1885. https://doi.org/10.1038/s41467-020-15659-1.

Otero-García, M., Agustín-Pavón, C., Lanuza, E., and Martínez-García, F. (2016). Distribution of oxytocin and co-localization with arginine vasopressin in the brain of mice. Brain Struct. Funct. *221*, 3445–3473. https://doi.org/10.1007/s00429-015-1111-y.

Pencea, V., Bingaman, K.D., Wiegand, S.J., and Luskin, M.B. (2001). Infusion of brain-derived neurotrophic factor into the lateral ventricle of the adult rat leads to new neurons in the parenchyma of the striatum, septum, thalamus, and hypothalamus. J. Neurosci. *21*, 6706–6717.

Quintana, D.S., and Guastella, A.J. (2020). An allostatic theory of oxytocin. Trends Cogn. Sci. *24*, 515–528. https://doi.org/10.1016/j.tics.2020.03.008.

Rae, M., Lemos Duarte, M., Gomes, I., Camarini, R., and Devi, L.A. (2021). Oxytocin and vasopressin: signalling, behavioural modulation and potential therapeutic effects. Br. J. Pharmacol. https://doi.org/10.1111/bph.15481.

Renier, N., Wu, Z., Simon, D.J., Yang, J., Ariel, P., and Tessier-Lavigne, M. (2014). iDISCO: a simple, rapid method to immunolabel large tissue samples for volume imaging. Cell *159*, 896–910. https://doi.org/10.1016/j.cell.2014.10.010.

Resendez, S.L., Namboodiri, V.M.K., Otis, J.M., Eckman, L.E.H., Rodriguez-Romaguera, J., Ung, R.L., Basiri, M.L., Kosyk, O., Rossi, M.A., Dichter, G.S., and Stuber, G.D. (2020). Social stimuli induce activation of oxytocin neurons within the paraventricular nucleus of the hypothalamus to promote social behavior in male mice. J. Neurosci. *40*, 2282–2295. https://doi.org/10.1523/JNEUROSCI.1515-18.2020.

Rhodes, C.H., Morriell, J.I., and Pfaff, D.W. (1981). Immunohistochemical analysis of magnocellular elements in rat hypothalamus: distribution and numbers of cells containing neurophysin, oxytocin, and vasopressin. J. Comp. Neurol. *198*, 45–64. https://doi.org/10.1002/cne.901980106.

Romanov, R.A., Tretiakov, E.O., Kastriti, M.E., Zupancic, M., Häring, M., Korchynska, S., Popadin, K., Benevento, M., Rebernik, P., Lallemend, F., et al. (2020). Molecular design of hypothalamus development. Nature *582*, 246–252. https://doi.org/10.1038/s41586-020-2266-0.

Romanov, R.A., Zeisel, A., Bakker, J., Girach, F., Hellysaz, A., Tomer, R., Alpár, A., Mulder, J., Clotman, F., Keimpema, E., et al. (2017). Molecular interrogation of hypothalamic organization reveals distinct dopamine neuronal subtypes. Nat. Neurosci. *20*, 176–188. https://doi.org/10.1038/nn.4462.

Roubertoux, P.L., Ghata, A., and Carlier, M. (2018). Measuring preweaning sensorial and motor development in the mouse. Curr. Protoc. Mouse Biol. *8*, 54–78. https://doi.org/10.1002/cpmo.41.

Smith, C.J.W., DiBenedictis, B.T., and Veenema, A.H. (2019). Comparing vasopressin and oxytocin fiber and receptor density patterns in the social behavior neural network: implications for cross-system signaling. Front. Neuroendocrinol. *53*, 100737. https://doi.org/10.1016/j.yfrne.2019.02.001.

Song, Z., and Albers, H.E. (2018). Cross-talk among oxytocin and arginine-vasopressin receptors: relevance for basic and clinical studies of the brain and periphery. Front. Neuroendocrinol. *51*, 14–24. https://doi.org/10.1016/j.yfrne.2017.10.004.

Stoop, R. (2012). Neuromodulation by oxytocin and vasopressin. Neuron *76*, 142–159. https://doi.org/10.1016/j.neuron.2012.09.025.

Sunkin, S.M., Ng, L., Lau, C., Dolbeare, T., Gilbert, T.L., Thompson, C.L., Hawrylycz, M., and Dang, C. (2012). Allen Brain Atlas: an integrated spatio-temporal portal for exploring the central nervous system. Nucleic Acids Res. *41*, D996–D1008. https://doi.org/10.1093/nar/gks1042.

Todrank, J., Busquet, N., Baudoin, C., and Heth, G. (2005). Preferences of newborn mice for odours indicating closer genetic relatedness: is experience necessary? Proc. Biol. Sci. *272*, 2083–2088. https://doi.org/10.1098/rspb.2005.3187.

Vaidyanathan, R., and Hammock, E.A.D. (2017). Oxytocin receptor dynamics in the brain across development and species. Dev. Neurobiol. *77*, 143–157. https://doi.org/10.1002/dneu.22403.

Veenema, A.H., and Neumann, I.D. (2008). Central vasopressin and oxytocin release: regulation of complex social behaviours. Prog. Brain Res. *170*, 261–276. https://doi.org/10.1016/S0079-6123(08)00422-6.

Verdaasdonk, J.S., Lawrimore, J., and Bloom, K. (2014). Determining absolute protein numbers by quantitative fluorescence microscopy. Methods Cell Biol. *123*, 347–365. https://doi.org/10.1016/B978-0-12-420138-5.00019-7.

Wang, Q., Ding, S.-L., Li, Y., Royall, J., Feng, D., Lesnar, P., Graddis, N., Naeemi, M., Facer, B., Ho, A., et al. (2020). The allen mouse brain common coordinate framework: a 3D reference atlas. Cell *181*, 936–953.e20. https://doi.org/10.1016/j.cell.2020.04.007.

Whitnall, M.H., Key, S., Ben-Barak, Y., Ozato, K., and Gainer, H. (1985). Neurophysin in the hypothalamo-neurohypophysial system. II. Immunocytochemical studies of the ontogeny of oxytocinergic and vasopressinergic neurons. J. Neurosci. *5*, 98–109.

Yamamoto, Y., Cushing, B.S., Kramer, K.M., Epperson, P.D., Hoffman, G.E., and Carter, C.S. (2004). Neonatal manipulations of oxytocin alter expression of oxytocin and vasopressin immunoreactive cells in the paraventricular nucleus of the hypothalamus in a gender-specific manner. Neuroscience *125*, 947–955. https://doi.org/10.1016/j.neuroscience.2004.02.028.

Yoo, S., and Blackshaw, S. (2018). Regulation and function of neurogenesis in the adult mammalian hypothalamus. Prog. Neurobiol. *170*, 53–66. https://doi.org/10.1016/j.pneurobio.2018.04.001.

Zheng, J.-J., Li, S.-J., Zhang, X.-D., Miao, W.-Y., Zhang, D., Yao, H., and Yu, X. (2014). Oxytocin mediates early experience-dependent cross-modal plasticity in the sensory cortices. Nat. Neurosci. *17*, 391–399. https://doi.org/10.1038/nn.3634.

STAR★METHODS

KEY RESOURCES TABLE

REAGENT or RESOURCE	SOURCE	IDENTIFIER
Antibodies		
Anti-Oxytocin (Host Rabbit)	Phoenix Pharmaceutical	Cat# G-051-01
Anti-Vasopressin Neurophysin II (AVP-NPII) (Host Mouse)	Merck Millipore	RRID:AB_2819363
Anti-Vasopressin (Host Rabbit)	Phoenix Pharmaceutical	Cat# G-065-07
Goat anti-Mouse IgG 647nm	Abcam	RRID:AB_2687948
Goat anti-Rabbit IgG 568nm	Abcam	RRID:AB_2576207
Chemicals, peptides, and recombinant proteins		
Paraformaldehyde 16%	Thermoscientific	Cat# 28908
Phosphate Buffer Saline 10-X	Roche	Cat# 11666789-001
Triton X-100	Sigma	Cat# 9002-93-1
Thimerosal	Sigma	Cat# 54-64-8
Methanol	VWR	Cat# 67-56-1
Saponin	Sigma	Cat# 804715-2
Gelatin	VWR	Cat# 9000-70-8
Dichloromethane	Sigma	Cat# 75-09-2
Dibenzylether	Sigma	Cat# 103-50-4
Experimental models: Organisms/strains		
Mouse: C57BL6/J	Charles River	Strain code: 027
Software and algorithms		
Imaris software	Oxford Instrument	Version 9.5
Prism	GraphPad Software	Version 8
Codes and algorithms	Oxytocin and Vasopressin Neurodevelopment Project	https://doi.org/10.17605/OSF.IO/39THQ
Other		
Peristaltic Pump	Cole Parmer	MasterFlex 7518-00

RESOURCE AVAILABILITY

Lead contact

Further information and requests for resources and reagents should be directed to and will be fulfilled by the lead contact: Angela Sirigu (angela.sirigu@isc.cnrs.fr).

Materials availability

This study did not generate new unique reagents or materials.

Data and code availability

- Microscopy data reported in this paper will be shared by the lead contact upon request.
- All original Matlab codes written to process and analyze the immunolabeled cells detected with the Imaris software have been posted on the Open Science Framework website as part of the Oxytocin and Vasopressin Neurodevelopment project, and are publicly available as of the date of publication. DOIs are listed in the key resources table.
- Any additional information required to reanalyze the data reported in this paper is available from the lead contact upon request.

EXPERIMENTAL MODEL AND SUBJECT DETAILS

Animal manipulations followed the guidelines of the European legislation for animal experimentation (directive 2010/63/EU) and were approved by the local institutional ethical committee (C2EA-UCBL55; project 2017112317077317). Adult C57BL/6J male and pregnant multiparous C57BL/6J female used in the study were obtained from Charles River (Arbresles, France). Once arrived at the animal facility, animals were weighted, earmarked for identification and group-housed (4 animals per cage), and left undisturbed at least one week before any manipulation. All animals were housed in transparent ventilated cages (under constant temperature of 23°C and 55% humidity), in an animal room with a 12-h light-dark cycle schedule (lights on at 7:00 a.m.), with free access to food, water, shelter and nesting materials. As maternal care can impact growth, neural development and behavioral outcomes in offspring (Curley and Champagne, 2016; Franks et al., 2015), female were left undisturbed to minimize perinatal stress. However, at gestational day 16, females were singly housed and were daily checked (twice a day) for the presence of pups from the outside of the cages. The day of delivery ~4 h after birth, designated as postnatal day (P0), newborn pups were weighted and litter size was adjusted to 5–6 pups per litter to normalize offspring access to maternal feeding resources and care (Enes-Marques and Giusti-Paiva, 2018). All animals were left undisturbed, except weekly weight measurements and cage changes until euthanasia. Just before intracardiac perfusion, pups (from PD0 to PD14), were weighted again, and a phalanx from the right fore paw toe was dissected for genetic determination of male gender by qPCR analysis of Sry gene expression (sex determining region Y, Gene ID: 25221 (Morikawa et al., 2011). However, since there was no difference in the total cell number expressing OXT and AVP between male and female (n = 2–3 male and n = 2–3 female per age group; two-way ANOVA: *OXT*: Gender effect F (3,10) = 3.594, p = 0.0872; Age effect F (3,10) = 116.2, p <0.0001; Interaction F (3,10) = 0.5404, p = 0.6654; *AVP*: Gender effect F (3,10) = 2.652, p = 0.1345; Age effect F (3,10) = 0.6056, p = 0.6262; Interaction F (3,10) = 1.654, p = 0.2390), data from female and male were pooled together (P0: n = 6; P3: n = 4; P7: n = 4; P14 n = 4). To avoid disrupting social environment by retrieving pups during development and sibling interaction within the same litter, offspring from the same cage were entirely euthanized at either P0, P3, P7 or P14. Adult male mice were between 56 and 77 days old at time of sacrifice (noted as ≥P56). The time scale used was specifically chosen to examine OXT and AVP neural organization during sensitive developmental phases covering the early postnatal phase, from the first day after birth (P0), neonate (P3 and P7) and infant (P14). Adult animals (≥ P56) were included as the final end point of the developmental curve.

METHOD DETAILS

Intracardiac perfusion

All animals were deeply anaesthetized using a mixture of ketamine (100 mg/kg body weight) and xylasine (5 mg/kg body weight, Virbac France) overdose injected intraperitoneally, and transcardially perfused first with a 0.1 M PBS solution (5 mL per animal for pups; 15 mL per animal for PD14 and adult mice), followed by tissue fixation with a cold 4% paraformaldehyde solution (ThermoFisher, France) diluted in 0.1 M PBS (15 mL for P0, D3 and P7 pups; 25 mL for P14 animals; 40 mL for adult mice). The brains were immediately extracted, post-fixed for an additional 12 h by immersion in 4% paraformaldehyde solution and stored in cold 0.1 M PBS solution until further use for immunofluorescence labeling and clearing procedures.

Whole brain pre-processing and immunofluorescence labeling

Whole brain labeling was performed following the iDISCO+ protocol initially described in (Renier et al., 2014). Perfused brains were washed in PBS 1X twice 30 min, and dehydrated in an increasing series of methanol in water washes (Sigma-Aldrich, France) (20%, 40%, 60%, 80%, 100%) for 1 h each. An additional wash of 1 h in methanol 100% was done to remove residual water. Samples were then incubated overnight in a solution containing a 66% dichloromethane (Sigma-Aldrich, Germany) in methanol with gentle shaking, and then washed twice in methanol 100% (1 h each). Once dehydrated, samples were bleached overnight at 4°C in methanol containing a 5% of hydrogen peroxide (Sigma-Aldrich, Germany) in the dark without shaking. Brains were finally rehydrated in a series of methanol 80%, 60%, 40% and 20% (1 h each wash) and washed in water for 30 min. To initiate immunostaining, pretreated samples were incubated for permeabilization in a PBS1X solution containing 0.2% gelatin (Sigma-Aldrich) and 0.5% of Triton X-100 (Sigma-Aldrich) (PBSGT) for 48 h at 37°C with shaking. Tissue samples were then blocked with the same PBSGT solution, by adding 5% of normal goat serum (JacksonImmunoResearch, UK) for 3 days at 37°C with gentle shaking. Samples were then washed in PBSGT containing 0.1% saponin with heparin (10 mg/ml) for 1 h to remove excess blood in the tissue. A PBSGT containing 0.1% saponin and normal goat serum

1% was used to prepare the antibodies solution. The following primary antibodies was used: mature Oxytocin (rabbit OXT, Phoenix Pharma Inc, France, #G-051-01, 1:400), mature AVP (rabbit AVP, Phoenix Pharma Inc, France, #G-065-07, 1:400) and AVP-neurophysin II (mouse AVP, MerckMillipore, Germany, #MABN845, clone PS41; 1:500). Based on literature and as indicated by the manufacturers, the primary neuropeptides did not cross-react with each other and with other hypothalamic peptides (Ben-Barak et al., 1985; Godefroy et al., 2017; Whitnall et al., 1985). Primary antibodies were incubated for 7 days (P0 and P3), 14 days (P7 and P14) or 21 days (adult) at 37°C with gentle shaking, then washed in PBS 1X (6 times 1 h and then overnight), and finally incubated for 2 days with secondary antibodies (Alexa Fluor goat anti rabbit 568, Abcam, UK, #ab175471; goat anti-mouse 647, Abcam, UK, #ab ab150115), at 1:800 dilution in PBSGT solution.

Tissue clearing

Following whole-brain immunolabeling, the samples were washed in PBS 1X (6 times 1 h and then overnight), dehydrated in a methanol/water increasing concentration series (20%, 40%, 60%, 80%, 100% one hour each and then methanol 100% overnight), followed by a wash in 66% dichloromethane–33% methanol for 3 h, followed by two washes in dichloromethane 100% (15 min each). Samples were finally cleared and stored in dibenzyl ether (Sigma-Aldrich) until light sheet imaging.

Light-sheet microscopy imaging settings

3D volume imaging was performed using an Ultramicroscope II (Mylteny), equipped with an Andor CMOS sNEO camera, an LVMI-Fluor 6.3X/O.3 WD6 LaVision Biotec objective, and a 5.7 mm working distance corrected dipping cap (magnifications ranging from 1.3X to 12.3 X with variable zoom). Depending on the region of interest, cleared brains were mounted either into a coronal (PVN, preoptic region, BNST, AMY) or horizontal (SON, TU) orientation and submerged in a 100% DBE reservoir. Two lasers were used per samples: a 561-nm laser for the detection of Alexa Fluor-568, and a 640-nm laser for Alexa Fluor-647-conjugated antibodies. Laser power and exposure times varied depending on the proximity of the signal to the surface of the sample, but were usually set to 10–20% for the 561-nm lasers and up to 30% for the 640-nm laser, with a 100–150 ms exposure time. The light sheet numerical aperture was set to its maximum value (0.156), with a light sheet width of 60% to ensure even illumination in the Y axis. Other imaging parameters (optical zoom, horizontal focusing, voxel size) were adjusted to the crop size. For hypothalamic scanning (from the anterior commissure to the median eminence), in coronal plane, a step size corresponding to the x and y pixel size was used to obtain approximatively cubic voxels: X:1.89; Y: 1.89; Z: 2 (optical zoom of 1.6) for adult samples; 1.51μm^3 (optical zoom of 2) for P14 and 1.21 μm^3 (optical zoom of 2.5) for P0, P3 and P7 samples. For region quantification, cellular details were obtained using a most zoomed acquisition onto the regions of interest, resulting in voxel size of 0.485 μm^3, 0.604 μm^3, or 0.75 μm^3. For all specimens, 2048 × 2048 pixel resolution, and 16-bit images were collected, resulting in datasets ranging from 30 to 150 Gigabytes (depending on voxel size, crop size, and number of channels used). Pilot studies dedicated to the imaging parameters settings revealed that a combination of excessive exposure time, and laser power can lead to a cross-reactivity of adjacent fluorophores, where the specific labeling expressed in the 488 nm wavelength for example could also be seen in the 568 nm channel, resulting in false-positive co-staining. To prevent such spectral overlap between the fluorochromes and minimize the fluorescence spill-over, we adjusted the immunolabeling protocols (signal intensity and specificity), by using different antibodies concentration and duration, and lack of one primary over the two primary antibodies used (data not shown).

QUANTIFICATION AND STATISTICAL ANALYSIS

Cell detection, cell quantification and region identification

Detection and quantification of OXT- and AVP-Ir cell bodies was realized in the entire brains (both hemispheres) using the spot detection module from Imaris software (version 9.5, Bitplane, Oxford Instrument). As a first step, cell diameter was set to 10 micrometers for automatic detection. This parameter was sufficient to avoid automatic detection of large vesicles. In a second step, manual verification and validation for each data sets were realized to discard any false positive or dismissed signals (i.e one spotted cells instead of two). Following detection, regions of interests (ROI) were defined based on cell density. For the hypothalamic nuclei, we first identified the Paraventricular nuclei (PVN) as the ROI#1, as this region contains the highest number of OXT and AVP cells localization in histological papers. From the Allen Mouse brain atlas (P56, coronal; slices 56 to 66) the PVN extends over about 1275 microns, from the beginning of anterior

commissure. The ROI#2 was identified as the SON, which stands in the ventral part of the hypothalamus, along the optic tract on 1150 microns (slices 56 to 65), with a fusiform shape. AVP staining was also found in the suprachiasmatic nucleus in addition to the PVN and SON, but the quantification in this brain region was not realized due to blurred aspect of the cells of high densities. The staining in this brain region was particularly diffuse and accurate cell counting between two blind experimenters was difficult to obtain. We next identified a postero-ventral region (ROI#3), with a high density, which was later aligned and annotated to the tuberal nucleus. This ROI begins with the end of the SON in the antero-posterior axis. The ROI#4 contained only OXT-Ir cells and was localized between the anterior commissure and the paraventricular nucleus, besides the third ventricle. This region corresponds to the ALPO after the atlas registration. ROI#5 was localized along the third ventricle before the PVN, from the ventral surface to the same dorsal level of the PVN in dorso-ventral axis; and corresponds to the periventricular (PvPO). ROI#6 contained dispersed cells, which corresponds to the accessory nuclei, localized between the SON and PVN. ROI#7 contains dispersed cells laterally and anteriorly to the PVN that was aligned to the median preoptic nucleus (MPN). For extra-hypothalamic regions, we detected cells the medial amygdala (MEA, ROI#8), located beyond the optic tract over 100 microns. In ROI#9 (BNST), cells were located above the anterior commissure. From the hypothalamic scanning, we obtained a list of nine regions containing OT and AVP cells, whose Cartesian coordinates in x, y, z were extracted to perform atlas registration and molecular volume estimation. We performed additional acquisitions for each identified ROIs to reach a higher resolution for detailed cell count within each region. Cell count was done at a resolution of 0.48 μm^3 in both hemispheres. As no difference was noted between left and right hemispheres, datasets were pooled together, and expressed as the total number of Ir cells.

Mesoscopic analysis and image processing

Allen brain atlas registration. In order to create a common annotated anatomical space during development and adulthood, each acquisition was re-referenced according the volumetric Allen brain atlas (Wang et al., 2020) with the following procedure:

Preprocessing. For each region and each acquisition, the occupancy volume was estimated by creating a binary mask in a space consisting of 25 μm voxels to match the resolution of the Allen brain atlas used as a reference space. The number of cells included in each voxel was counted and the resulting matrix was smoothed using a Gaussian filter of standard deviation 50 μm. This procedure is equivalent to a kernel density estimation. The resulting density is then unity-based normalized by dividing all voxels by the maximum density and the final binary mask is obtained by thresholding the 3D image obtained with a threshold of 0.1.

Anatomical landmarks. In order to validate and better define the location of the different pre-identified ROIs, each data acquisition was transposed into the reference atlas using the PVN and SON occupancy volumes as reference anatomical landmarks. First, for the adult animals, the molecular volumes occupied by the OXT-Ir and AVP-Ir cells were combined and symmetrized with respect to the sagittal plane. Then, atlas registration was processed using rigid transformations (only scale, position and rotation were estimated) using custom MATLABMatlab code to align the obtained volumes within the PVN and SON volumes of the Allen Brain Mouse Atlas. PVN and SON were chosen as our internal anatomical reference landmarks because they are the two regions with the best signal-to-noise ratio and the OXT-Ir and AVP-Ir neurons are sufficient to estimate the full volume of these two regions. Moreover, the PVN and the left and right SON constitute three distant points in the acquisition volume that are perfectly adapted to obtain an accurate alignment of the whole acquisition volume in the reference space. After alignment, there is an average 11% shrinkage in volume compared to the reference atlas. This contraction rate is then taken into account for all analyses.

Developmental atlas. To compare datasets obtained from different mice, onto a common 3D coordinate space, all acquisitions were re-referenced in an adult space based on the Allen brain mouse atlas. Acquisitions on younger animals were registered in the same space using the same procedure but using the aligned, combined, and symmetrized PVN and SON volumes of the older animals as the new landmarks. Thus, adult's animals ($\geq$P56) were re-referenced according to the Allen-Brain Atlas, juveniles (P14) according to adults, infants (P7) according to juveniles, neonates (P3) according to infants, and early post-natal acquisitions (P0) according to neonates. This procedure allows to estimate the global scale change of the studied region from birth to adulthood and to minimize the alignment errors of the structures that may evolve in their shape during development.

Single-cell processing and 3D modeling

Intra- and inter-groups modeling (point cloud registration within and across age groups). For analyses that focus on a single region (i.e PVN) point-set registration was preferred over classical atlas/volume-based registration to preserve the full spatial resolution of the acquisitions. Point cloud registration is particularly suitable for the analysis of cell detection in light sheet microscopy because it allows to efficiently merge acquisitions made on several animals directly in three dimensions without transformation of the data and consequently minimizing the risk of modifying cell architecture. Coherent Point Drift Algorithm (CPD) (Myronenko and Song, 2010) was used for this purpose using the first author Matlab implementation (CPD ver.2) focusing on rigid point set registration and matching. First, the detections of OXT-Ir and AVP-Ir cells of an arbitrary adult animal (P56) were combined, centered and mirror symmetrized with respect to the sagittal plane in order to constitute an arbitrary reference space focused on the region of interest (Figures S4A–S4C). Then, each adults' animals ($\geq$ P56 n = 6) were transposed in the reference space using CPD with rigid point set registration (Figure S4D). Finally, all estimated scale parameter were averaged and all re-referenced coordinates were multiplied by this value in order to obtain a structure with dimensions of an average adult animal. Then, for younger animals, the same procedure that was described before was applied. The mirror symmetrized re-referenced adult coordinates was used as a reference to align juveniles (P14), infants (P7) were re-referenced according to juveniles, neonates (P3) according to infants, and birth acquisitions (P0) according to neonates. Finally, the set of estimated scaling parameters were then recorded as measures of the evolution of structure size during the development and a scale correction procedure was used to visualize the growth of the region (Figure S4E).

Cell-based density clustering. Once point cloud set, local/zonal density can be estimated at any location using K-nearest neighbor's algorithm. During brain development, two independent parameters influence the density measurements: the evolution of the global size of the structure due to the growth of the animal and the evolution of the structure itself due to the dynamics of cellular expression. As we focus on the ontogeny of OXT cell expression in the PVN, changes in cell density due to global size growth were controlled by using data re-referenced in the adult dimension space (Figure S4D). Then, to quantitatively measure the evolution of the density during the development, a measurement space constituted by the coordinates of all the cells detected in the adult subjects was defined. Then for each coordinate within this measurement space, the local density was estimated for each age, by calculating the average distance between the measurement point and the K nearest referenced cells (K = 100 - for a measurement space consisting of the OXT cells detected for 3 animals to which we add the same data in mirror symmetry; the average distance D of the K nearest neighbors can be converted in density, considering that in a sphere of radius D, the expected number of cells is K/2). In this study, densities are systematically reported in number of cells/cube of 100 μm of side per animal. By subtracting the density values at P0 from the adult density values it can be seen that, OXT cell density increases with age, as expected, with the exception of areas, located in the postero-dorsal part, where density seems stable or decreasing (Figure S4F). Two binary masks were then generated using the method described above to generate two regions of interest in the PVN for future analysis (Figure S4F, last panel). Finally, an OXT cell count was performed for each animal in the two clusters and an analysis of variance were used to attest the increase, stability or decrease of the number of cells in the two PVN partitions considered.

Cell-based fluorescence intensity analysis. For each identified cell, the fluorescence intensity value was estimated, based on the peak intensity voxel, since this method does not assume a constant volume via Imaris Software (Bitplane, Oxford Instrument). Imaging parameters were set to minimize photobleaching image acquisition (Coffman and Wu, 2012; Verdaasdonk et al., 2014). As the fluorescence values are not directly comparable between two acquisitions and as the objective of this analysis is to identify fluorescence variations within the PVN, the fluorescence values were systematically Z-transformed for each subject (Figure S4G). Finally, using the two PVN subdivisions obtained by cell density analyses, for each animal the average difference in fluorescence between the two regions was estimated and an analysis of variance with post-hoc test corrected by the Tukey-Kramer's post-hoc correction for multiple comparisons was used to identify periods in development when a difference in fluorescence between the two clusters can/could be observed.

Statistical analysis

The statistical analysis and graphical representations were performed using GraphPad Prism 8 software (GraphPad Software, Inc). Comparisons within groups (for OXT or AVP) were determined by either

one-way ANOVA (age effect) or two-way ANOVA (age x region). Tukey-Kramer's multiple comparisons test was used to find post hoc differences among groups and calculate 95% confidence intervals to report effect size. When 95% confidence intervals were not calculated, then the Holm-Sidak's multiple comparisons test was used. In the text and figures, values are provided as mean $\pm$ SEM, and $p < 0.05$ was set as the criterion for statistical significance.